Polarized Raman scattering from single GaP nanowires

Jian Wu,[1,*,†] Duming Zhang,[1,*,‡] Qiujie Lu,[1] Humberto R. Gutierrez,[1,*,§] and Peter C. Eklund[1,2]
[1]*Department of Physics, The Pennsylvania State University, University Park, Pennsylvania 16802, USA*
[2]*Department of Materials Science and Engineering, The Pennsylvania State University, University Park, Pennsylvania 16802, USA*
(Received 23 September 2009; revised manuscript received 23 February 2010; published 8 April 2010)

We report the systematic investigation of polarized Raman scattering on individual crystalline GaP nanowires (NWs) with diameters $40<d<600$ nm. At small diameter, $d<70$ nm, the NWs are found to act like a nearly perfect dipole antenna that leads to a polarized scattering intensity function $I(\theta)\sim\cos^4\theta$ where θ is the angle between NW axis and the incident laser polarization. For larger diameter ($70<d<600$ nm) NWs, some other different polar patterns were found. A simple theoretical approach which takes into account the Raman tensor and photon confinement in NWs was used to understand the experimental data.

DOI: 10.1103/PhysRevB.81.165415 PACS number(s): 33.20.Fb, 78.67.Lt

I. INTRODUCTION

The last two decades have witnessed the growth of interests on semiconductor nanowires (SNWs) due to their wide range of applications and their potential as one of the next generation building blocks for nanoscale electronics,[1] photonics,[2] or sensors.[3] One of the most interesting properties for SNWs is quantum confinement. Because of the confinement of electrons, the band gap increases as the SNW size decreases.[4,5] Phonon confinement, for an example, has also been clearly identified for the asymmetric broadening of Raman spectra from Si NWs with diameters smaller than 10 nm.[6] When light interacts with SNWs, photons can also be trapped or confined by these dielectric filaments[7,8] because their size is comparable to the wavelength of light. Recently, strong resonance effects caused by photon confinement have been observed in both elastic[9] and Raman scattering[10–12] from SNWs.

In this paper, we will show how the photons confined inside GaP NWs change the polarized Raman scattering from semiconductors at the nanoscale. Polarized Raman scattering experiments have been carried out from single WS_2 (Ref. 13) nanotubes, and SiC and wurtzite GaN NWs.[14] Optical antenna effect observed from 20-nm-diameter WS_2 nanotubes by Resonant Raman scattering was attributed to the screening of polarizability.[13] However, complex-valued Raman tensor was proposed to explain the experimental polarized Raman data on single GaN nanowires.[14] Comparing with the abundant literature results in single-carbon nanotube Raman spectroscopy,[15,16] little or no systematic studies on single SNW Raman spectroscopy have been done.

We use cubic GaP NWs with diameters $40<d<600$ nm as a test bed to investigate the first-order polarized Raman scattering from single SNWs. All GaP NWs studied in this report were synthesized by pulsed laser vaporization. Transmission electron microscope (TEM) analysis show that these GaP NWs are highly crystalline and only two growth directions, ⟨110⟩ and ⟨111⟩, were found. The detailed synthesis and characterization information has been published elsewhere.[17] In Fig. 1(a) we display a typical Raman spectrum of an individual GaP NW showing two main peaks of transverse optical phonon (TO, ~356 cm^{-1}) and longitudinal optical phonon (LO, ~392 cm^{-1}) scattering. A weaker Raman band (~385 cm^{-1}) also appears on the lower-frequency side of the LO phonon peak. This is due to scattering from surface optical (SO) modes activated by surface roughness and/or faceting on the NW surface.[18] We will, however, not discuss SO mode in this work. GaP NWs provide us an ideal candidate over the other SNWs systems given that (1) they are easy to grow, (2) the single-wire Raman spectrum has excellent signal to noise ratio in tens of seconds at excitation laser wavelength 514.5 nm and small laser power ~2 mW, and (3) GaP NWs have cubic structure which Raman tensors are much more simpler than wurtzite semiconductors, such as GaN.

The following context is organized by four sections: we first review Raman scattering from bulk semiconductors, both the experimental and theoretical results on the polarized Raman scattering on bulk GaP [100] and [111] are shown; then the procedures and results on NW Raman tensor calculations are presented; thirdly a simple theory based on bulk Raman scattering and photon confinement is proposed and finally experimental polarized Raman scattering from GaP NWs are discussed and compared with the proposed theory.

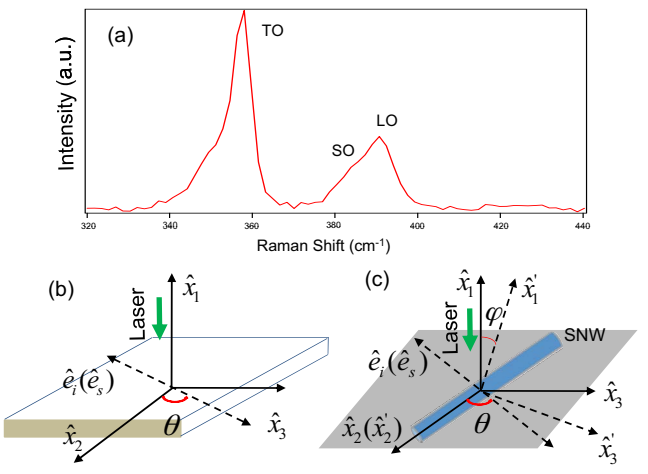

FIG. 1. (Color online) (a) A Raman spectrum of GaP NWs. (b) Schematic of polarized Raman scattering on cubic (b) bulk GaP wafer and (c) GaP NWs. The arrow indicates the direction of the excitation laser. $\hat{e}_i$ and $\hat{e}_s$ are the incident and scattered light polarizations, respectively.

II. POLARIZED RAMAN SCATTERING FROM BULK CUBIC GaP

Let us first review Raman scattering from bulk semiconductors. It is well known that the TO and LO Raman intensities I_s, where the subscript s represents either TO or LO, are dependent on the polarization of incident radiation $\hat{e}_i$, the polarization of scattered radiation $\hat{e}_s$, and the Raman tensor $\tilde{\Re}(s)$. It can be written as in Refs. 18 and 19

$$I_s \propto \omega^4 I_0 |\hat{e}_s \cdot \tilde{\Re}(s) \cdot \hat{e}_i|^2, \tag{2.1}$$

where ω and I_0 are the frequency and intensity of incident light, respectively. The form of the Raman tensor $\tilde{\Re}$ is related to the symmetry of Raman-active phonons. For semiconductors with the zinc-blende structure, the Raman tensors for optic phonons with atomic displacements along the $\langle 100\rangle$, $\langle 010\rangle$, and $\langle 001\rangle$ crystallographic axes are[19,20]

$$\tilde{\Re}(\hat{e}_1) = \begin{bmatrix} 0 & 0 & 0 \\ 0 & 0 & a \\ 0 & a & 0 \end{bmatrix}, \tilde{\Re}(\hat{e}_2) = \begin{bmatrix} 0 & 0 & a \\ 0 & 0 & 0 \\ a & 0 & 0 \end{bmatrix}, \tilde{\Re}(\hat{e}_3) = \begin{bmatrix} 0 & a & 0 \\ a & 0 & 0 \\ 0 & 0 & 0 \end{bmatrix}, \tag{2.2}$$

where the unit vectors $\hat{e}_m$ $(m=1,2,3)$ represent the $\langle 100\rangle$, $\langle 010\rangle$, and $\langle 001\rangle$ axes, respectively. We use the subscript m to distinguish them from the polarizations of incident and scattered lights $\hat{e}_i$ and $\hat{e}_s$. The constant a in the tensors takes on different values for TO and LO phonons.

Let us consider the scattering geometry of a bulk semiconductor slab in Fig. 1(b). We are primarily interested in the change in the backscattered intensity as the incident polarization is rotated by θ about the incident photon wave vector $\vec{k}_i$. The laser with wavelength 514.5 nm (Coherent Innova 70C) is directed along the $-\hat{x}_1$ direction of the lab $(\hat{x}_1,\hat{x}_2,\hat{x}_3)$ coordinate system and focused by the microscope objective onto the sample plane $(\hat{x}_2,\hat{x}_3)$. The laser polarization $\vec{E}_0$ is initially polarized along the $\hat{x}_2$ axis. As it passes through a rotatable half wave plate (HWP), the laser polarization will be rotated by an angle θ in the horizontal plane.[14,21] The backscattered light from the sample propagates along the $\hat{x}_1$ direction and is collected by the objective lens and then passes again through the polarization rotator where the electric vector is counter-rotated by the angle θ. The analyzer, positioned before the entrance slit, is fixed to only pass the scattered E-field component parallel to the polarization of the incident laser. Finally the light coming out of the spectrometer is collected by an air-cooled charge-coupled device.

Depending on the orientation of the HWP, the polarization direction for the incident $\hat{e}_i$ and backscattered radiation $\hat{e}_s$ is

$$\hat{e}_i = \hat{e}_s = \begin{pmatrix} 0 \\ \cos\theta \\ \sin\theta \end{pmatrix} = \hat{e}. \tag{2.3}$$

The wave vectors for the incident and backscattered radiation, $\hat{k}_i$ and $\hat{k}_s$, respectively, are both parallel to the $\hat{x}_1$ axis. To comply with the photon-phonon wave-vector conservation rule, the wave vector of the optical phonon $\hat{q}$ excited in the Raman process must also be parallel to the $\hat{x}_1$ axis (the phonon wave vector is $q=2k_i$). Therefore, the displacement of the LO phonons must be along the $\hat{x}_1$ axis and the displacement of the TO phonons must be perpendicular to the $\hat{x}_1$ axis. Then from Eqs. (2.3) we have for scattering from the bulk that

$$I^{\mathrm{LO}}_{\mathrm{bulk}}(\theta) \propto |\hat{e} \cdot \tilde{\Re}(\hat{x}_1) \cdot \hat{e}|^2 \tag{2.4a}$$

and

$$I^{\mathrm{TO}}_{\mathrm{bulk}}(\theta) \propto \left| \hat{e} \cdot \frac{1}{\sqrt{2}} \tilde{\Re}(\hat{x}_2) \cdot \hat{e} \right|^2 + \left| \hat{e} \cdot \frac{1}{\sqrt{2}} \tilde{\Re}(\hat{x}_3) \cdot \hat{e} \right|^2, \tag{2.4b}$$

where the two terms in Eq. (2.4b) can be identified with two orthogonal TO phonons. These results predict the polarization dependence of the bulk TO and LO scattering.

Here we use Eqs. (2.4a) and (2.4b) to work out two examples, bulk GaP [100] and [111], to see how the first-order Raman-scattering intensities of optical-phonons change with the angle θ and compare our calculations with experiments.

For bulk GaP [100], we set the laboratory coordinates $\hat{x}_1$, $\hat{x}_2$, and $\hat{x}_3$ correspond to the three principle crystallographic axes $\langle 100\rangle$, $\langle 010\rangle$, and $\langle 001\rangle$, respectively, i.e.,

$$\tilde{\Re}(\hat{x}_m) = \tilde{\Re}(\hat{e}_m). \tag{2.5}$$

From Equations (2.4a), (2.4b), and (2.5), we have

$$I^{\mathrm{TO}}_{\mathrm{bulk\ GaP[100]}}(\theta) = 0 \quad \text{and} \quad I^{\mathrm{LO}}_{\mathrm{bulk\ GaP[100]}}(\theta) \propto \sin^2(\theta)\cos^2(\theta). \tag{2.6}$$

Notice that the TO intensity for GaP [100] is zero.

For bulk GaP [111], we set

$$\hat{x}_1 = [111], \quad \hat{x}_2 = [11\bar{2}], \quad \hat{x}_3 = [1\bar{1}0].$$

Then we have

$$\tilde{\Re}(\hat{x}_1) = \tilde{\Re}([111]) = \begin{bmatrix} \frac{1}{\sqrt{3}} & \frac{1}{\sqrt{3}} & \frac{1}{\sqrt{3}} \\ \frac{1}{\sqrt{6}} & \frac{1}{\sqrt{6}} & \frac{-2}{\sqrt{6}} \\ \frac{1}{\sqrt{2}} & \frac{-1}{\sqrt{2}} & 0 \end{bmatrix} \left\{ \frac{1}{\sqrt{3}} [\tilde{\Re}(\hat{e}_1) + \tilde{\Re}(\hat{e}_2) + \tilde{\Re}(\hat{e}_3)] \right\} \begin{bmatrix} \frac{1}{\sqrt{3}} & \frac{1}{\sqrt{6}} & \frac{1}{\sqrt{2}} \\ \frac{1}{\sqrt{3}} & \frac{1}{\sqrt{6}} & \frac{-1}{\sqrt{2}} \\ \frac{1}{\sqrt{3}} & \frac{-2}{\sqrt{6}} & 0 \end{bmatrix}, \tag{2.7a}$$

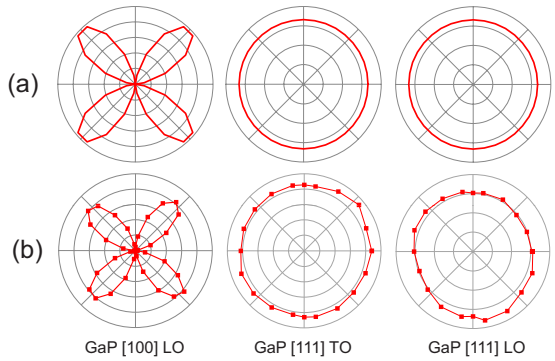

FIG. 2. (Color online) (a) Calculated intensity polar patterns of TO and LO phonons for bulk GaP wafer [100] and [111]. The TO intensity for [100] is zero according to Eq. (2.6) and it was supported by our experiments. (b) Experimental polar patterns of TO and LO phonons for bulk GaP [100] and [111]. The experimental data show excellent agreement with the theory.

$$\tilde{\Re}(\hat{x}_2)=\tilde{\Re}([11\bar{2}])=\begin{bmatrix}\frac{1}{\sqrt{3}} & \frac{1}{\sqrt{3}} & \frac{1}{\sqrt{3}}\\ \frac{1}{\sqrt{6}} & \frac{1}{\sqrt{6}} & \frac{-2}{\sqrt{6}}\\ \frac{1}{\sqrt{2}} & \frac{-1}{\sqrt{2}} & 0\end{bmatrix}\left\{\frac{1}{\sqrt{6}}[\tilde{\Re}(\hat{e}_1)+\tilde{\Re}(\hat{e}_2)-2\tilde{\Re}(\hat{e}_3)]\right\}\begin{bmatrix}\frac{1}{\sqrt{3}} & \frac{1}{\sqrt{6}} & \frac{1}{\sqrt{2}}\\ \frac{1}{\sqrt{3}} & \frac{1}{\sqrt{6}} & \frac{-1}{\sqrt{2}}\\ \frac{1}{\sqrt{3}} & \frac{-2}{\sqrt{6}} & 0\end{bmatrix}, \tag{2.7b}$$

$$\tilde{\Re}(\hat{x}_3)=\tilde{\Re}([1\bar{1}0])=\begin{bmatrix}\frac{1}{\sqrt{3}} & \frac{1}{\sqrt{3}} & \frac{1}{\sqrt{3}}\\ \frac{1}{\sqrt{6}} & \frac{1}{\sqrt{6}} & \frac{-2}{\sqrt{6}}\\ \frac{1}{\sqrt{2}} & \frac{-1}{\sqrt{2}} & 0\end{bmatrix}\left\{\frac{1}{\sqrt{2}}[\tilde{\Re}(\hat{e}_1)-\tilde{\Re}(\hat{e}_2)]\right\}\times\begin{bmatrix}\frac{1}{\sqrt{3}} & \frac{1}{\sqrt{6}} & \frac{1}{\sqrt{2}}\\ \frac{1}{\sqrt{3}} & \frac{1}{\sqrt{6}} & \frac{-1}{\sqrt{2}}\\ \frac{1}{\sqrt{3}} & \frac{-2}{\sqrt{6}} & 0\end{bmatrix}. \tag{2.7c}$$

Substituting the above Raman tensors in Eqs. (2.7a), (2.7b), and (2.7c) into Eqs. (2.4a) and (2.4b), we obtain

$$I^{\mathrm{TO}}_{\mathrm{bulk\ GaP[111]}}(\theta)=C_1 \quad \text{and} \quad I^{\mathrm{LO}}_{\mathrm{bulk\ GaP[111]}}(\theta)=C_2,$$

where C_1 and C_2 are both constants. Figures 2(a) and 2(b) show both the calculated and experimental data for bulk GaP [100] and [111], respectively. We call these intensity polar patterns or polar plots. In Fig. 2(b), the experimental data points are connected to guide the eyes. For GaP [100], both theory and experiment of LO mode show the quadruple patterns. They are circles for both TO and LO modes of GaP [111]. The theoretical calculations and experiments show excellent agreement with each other.

III. RAMAN TENSOR CALCULATION FOR GaP NWS

According to the above section, the Raman tensor determines the shapes of polar patterns of semiconductors. Therefore, we demonstrate how to calculate the Raman tensors of cubic GaP NWs with different growth directions and a specific orientation φ about the NW axis. Furthermore, we calculate the TO and LO intensity polar patterns for these NWs applying Eqs. (2.4a) and (2.4b).

The scattering geometry for NWs is shown in Fig. 1(c) which is almost exactly like what we described in Sec. II except the sample is changed from bulk slab to NWs. It is defined by introducing two coordinate systems: the lab coordinate system $(\hat{x}_1,\hat{x}_2,\hat{x}_3)$ and the crystal coordinate system $(\hat{x}'_1,\hat{x}'_2,\hat{x}'_3)$ attached to the NW. $\hat{x}'_2$ $(\hat{x}_2)$ is parallel to the NW growth axis; $\hat{x}'_1$ and $\hat{x}'_3$ are the other two crystallographic axes of the NW in the plane of $(\hat{x}_1,\hat{x}_3)$. Comparing with bulk semiconductor, there is another degree of freedom for SNWs called rotational angle φ. It is the angle between $\hat{x}_1$ and $\hat{x}'_1$ axes in the plane of $(\hat{x}_1,\hat{x}_3)$ as shown in Fig. 1(c).

First, we suppose that

$$\hat{x}'_k=\sum_m \alpha_{km}\hat{e}_m, \quad \hat{x}_k=\sum_m \beta_{km}\hat{x}'_m, \tag{3.1}$$

where k, $m=1,2,3$, and the $\hat{e}_m$ are defined in Sec. II. Then we can define two transformation matrices T' and T based, respectively, on the coefficients α_{km} and β_{km}

$$\mathrm{T}'=\begin{pmatrix}\alpha_{11} & \alpha_{12} & \alpha_{13}\\ \alpha_{21} & \alpha_{22} & \alpha_{23}\\ \alpha_{31} & \alpha_{32} & \alpha_{33}\end{pmatrix}, \tag{3.2a}$$

$$\mathrm{T}=\begin{pmatrix}\beta_{11} & \beta_{12} & \beta_{13}\\ \beta_{21} & \beta_{22} & \beta_{23}\\ \beta_{31} & \beta_{32} & \beta_{33}\end{pmatrix}=\begin{pmatrix}\cos\varphi & -\sin\varphi & 0\\ \sin\varphi & \cos\varphi & 0\\ 0 & 0 & 1\end{pmatrix}. \tag{3.2b}$$

The Raman tensors $\Re(\hat{x}'_k)$ for optical phonons displaced along the directions $\hat{x}'_k$ can then be written as

$$\tilde{\Re}(\hat{x}'_k)=\sum_m \alpha_{km}\Re(\hat{e}_m), \tag{3.3}$$

where the Raman tensors $\tilde{\Re}(\hat{e}_m)$ are given by Eq. (2.2). Then the Raman tensors for phonons displacements in the directions $\hat{x}'_k$ in the coordinate system $\{\hat{x}'_k\}$ are

$$\tilde{\Re}'(\hat{x}'_k)=\sum_m \alpha_{km}T'\cdot\tilde{\Re}(\hat{e}_m)\cdot T'^{-1}. \tag{3.4}$$

Similarly, we have the Raman tensors for optical phonons displaced along the direction $\hat{x}_k$ in the coordinate system $\hat{x}'_k$ and $\hat{x}_k$, given by

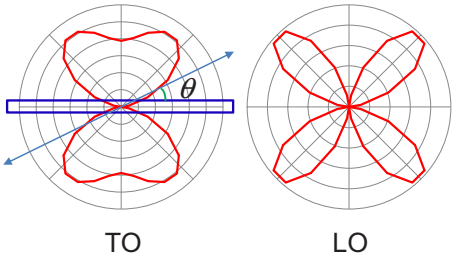

FIG. 3. (Color online) Calculated θ dependence of the contribution to the backscattered Raman intensity as seen at the detector for a $\langle 100\rangle$ GaP NW oriented along the $\hat{x}_2$ axis and taking into account *only* the contribution from the Raman tensor. Results are calculated according to Eq. (3.4) for angles φ between the $\langle 001\rangle$ direction and the $\hat{x}_1$ axis. From the calculation we found that the shape of the both TO and LO polar plots remain the same, independent of φ. The rectangle represents a NW.

$$\tilde{\Re}'(\hat{x}_k) = \sum_m \beta_{km} \tilde{\Re}'(\hat{x}'_k), \tag{3.5a}$$

$$\tilde{\Re}(\hat{x}_k) = \sum_m \beta_{km} T \cdot \tilde{\Re}'(\hat{x}_k) \cdot T^{-1}. \tag{3.5b}$$

Following the strategy above, we can calculate the Raman tensors $\tilde{\Re}(\hat{x}_k)$ for NWs with growth axis along $\langle 100\rangle$, $\langle 110\rangle$, and $\langle 111\rangle$, and for specific choices of the NW rotation angle φ. Then the TO and LO scattering intensities vs θ (polar plots) can be calculated by applying Eqs. (2.4a) and (2.4b).

The Raman tensor-based intensity polar patterns are shown in Figs. 3–5, respectively. A NW is represented schematically in Fig. 3; it is permanently oriented along θ=0°, where θ increases with counterclockwise rotation of the radial coordinate in the polar plot.

The tensor-based polar plots for GaP $\langle 100\rangle$ NW are the simplest, as shown in Fig. 3. The shapes of both TO and LO patterns stay the same, except for changes in intensity. For GaP $\langle 111\rangle$ NWs shown in Fig. 4, the polar patterns associated with LO phonon scattering do not change while the TO patterns display some variety for $0° \le \varphi \le 30°$; the polar patterns just repeat themselves for $30° \le \varphi \le 60°$ and again in $60° \le \varphi \le 90°$. Figure 5 shows the TO and LO polar patterns of GaP $\langle 110\rangle$ NWs for $0° < \varphi < 180°$. The variety of the tensor-based polar patterns seen in the figure indicates the sensitivity of the scattering pattern to the NW orientation about the $\langle 110\rangle$ growth axis.

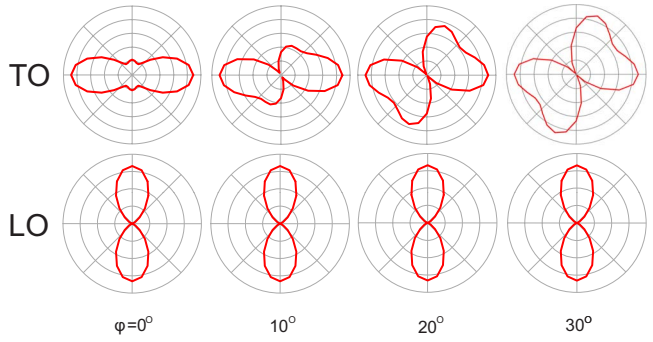

FIG. 4. (Color online) Calculated θ dependence of the contribution to the backscattered Raman intensity as seen at the detector for a $\langle 111\rangle$ GaP NW oriented along the $\hat{x}_2$ axis and taking into account only the contribution from the Raman tensor. Results are calculated according to Eq. (3.4) for angles φ between the $\langle 11\bar{2}\rangle$ direction and the $\hat{x}_1$ axis. It can be seen that the shape of the LO polar plot remains the same, independent of φ. The TO patterns change only from $0° < \varphi < 30°$, i.e., the patterns repeat every 30°.

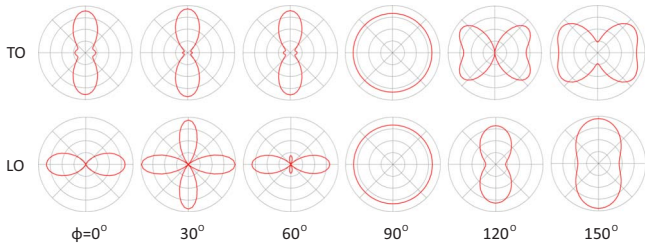

FIG. 5. (Color online) Calculated θ dependence of the contribution to the backscattered Raman intensity as seen at the detector for a $\langle 110\rangle$ GaP NW oriented along the $\hat{x}_2$ axis and taking into account only the contribution from the Raman tensor. Results are calculated according to Eq. (3.4) for angles φ between the $\langle 1\bar{1}1\rangle$ direction and the $\hat{x}_1$ axis. The shape of both the LO and TO polar plots shows the sensitivity depending on φ.

IV. THEORY OF RAMAN SCATTERING FROM SEMICONDUCTOR NANOWIRES

In this section, we present a theory to describe Raman scattering from SNWs considering the Raman tensor as well as photon-confinement effect. Consider again the scattering geometry shown in Fig. 1(c), i.e., a plane wave at wavelength λ is incident along $-\hat{x}_1$, where the NW lies in the $(\hat{x}_2,\hat{x}_3)$ plane with its axis along $\hat{x}_2$. The incident electric field from the laser external to the NW is given by

$$\vec{E}_0 = E_0 \hat{e}_i = \begin{pmatrix} 0 \\ E_0 \cos\theta \\ E_0 \sin\theta \end{pmatrix}, \tag{4.1}$$

where θ is the angle between the polarized laser field direction $\hat{e}_i$ and the NW axis which lies along $\hat{x}_2$. We denote the incident field *inside* the NW by $\vec{E}'_0$ which can be written as the product of a tensor $\tilde{Q}$ and the incident field outside the wire

$$\vec{E}'_0 = \tilde{Q} \cdot \vec{E}_0. \tag{4.2}$$

The form of $\tilde{Q}$ is taken to be diagonal

$$\tilde{Q} = \begin{pmatrix} 0 & 0 & 0 \\ 0 & Q_{\parallel} & 0 \\ 0 & 0 & Q_{\perp} \end{pmatrix}, \tag{4.3}$$

where $Q_{\parallel}$ and $Q_{\perp}$ refer to components parallel and perpendicular to the NW axis. $\tilde{Q}$ is introduced to describe the photon-confinement property of the NWs, i.e., how the electric field can be "squeezed" into the NWs. In general, $\tilde{Q}$ will

also be a function of position inside the NW. It can be shown, however, that the volume average of the tensor components $(Q_{\parallel}, Q_{\perp})$ is all that is required to compute the scattering.[9,11]

The scattered vector field $\vec{E}_s'$ inside the NW is defined by the application of a scattering matrix $\tilde{S}$ to the internal field $\vec{E}_0'$. That is, we have

$$\vec{E}_s' = \tilde{S} \cdot \vec{E}_0'. \tag{4.4}$$

For Raman scattering, the scattering matrix $\tilde{S}$ is the Raman tensor $\tilde{\mathfrak{R}}$, i.e., $\tilde{S}=\tilde{\mathfrak{R}}$.

The NW then emits an external field given by the product of an emission tensor $\tilde{Q}_e$ and the internal scattered field

$$\vec{E}_s = \tilde{Q}_e \cdot \vec{E}_s'. \tag{4.5}$$

We also make the usual simplification, i.e., $\tilde{Q}_e \simeq \tilde{Q}$ (Refs. 10, 22, and 23) because the Raman shift is small compared with incident laser. The polarization of the *detected* scattered electric field $\hat{e}_s$, is parallel to the incident field $\hat{e}_i$ (this follows from the experimental conditions). Then the external scattered intensity associated with this polarization can be written as

$$\begin{aligned} I_{\text{Raman}}^{\text{NW}} &\propto \omega^4 |\hat{e}_s \cdot \vec{E}_s|^2 = \omega^4 |\hat{e}_s \cdot \tilde{Q} \cdot \tilde{\mathfrak{R}} \cdot \tilde{Q} \cdot \vec{E}_0|^2 \\ &= \omega^4 |\hat{e}_s \cdot \tilde{Q} \cdot \tilde{\mathfrak{R}} \cdot \tilde{Q} \cdot \hat{e}_i|^2 I_0, \end{aligned} \tag{4.6}$$

where I_0 and ω are the intensity and frequency of external incident light, respectively. It is important to notice that the theory we present in this paper has two main differences from our previous publication.[11] First, in Eq. (4.6) the enhancement factor Q is considered as a tensor while in Ref. 11 we considered Q as a scalar. Second, in Ref. 11 the value of the Q was calculated from the field inside finite GaP NWs by discrete dipole approximation (DDA). Our more recent data shows that DDA calculations can only explain part of the experimental results. However if the Q factors are extracted from the experimental Rayleigh scattering data or from infinitely long-wire calculation, as shown in the present work, the theoretical model can better predict the experimental Raman polar patterns.

After transformations of T and T' in Eq. (3.5), the Raman tensor has the general form

$$\tilde{\mathfrak{R}} = \begin{bmatrix} R_{11} & R_{12} & R_{13} \\ R_{21} & R_{22} & R_{23} \\ R_{31} & R_{32} & R_{33} \end{bmatrix}.$$

Using Eq. (4.6), the scattered Raman intensity for SNWs then takes the form

$$\begin{aligned} I_{\text{Raman}}^{\text{NW}} \propto (&R_{22} Q_{\parallel}^2 \cos^2\theta + R_{23} Q_{\parallel} Q_{\perp} \cos\theta \sin\theta \\ &+ R_{32} Q_{\parallel} Q_{\perp} \cos\theta \sin\theta + R_{33} Q_{\perp}^2 \sin^2\theta)^2. \end{aligned} \tag{4.7}$$

The values of R_{ij} depend on the NW growth direction $\langle hkl \rangle$ and the "tipping" angle φ. The calculation has been shown in Sec. III. Equation (4.7), together with the appropriate values of $Q_{\parallel}$ and $Q_{\perp}$ can be used to predict the backscattered Raman-intensity pattern. Also we found that for Rayleigh scattering-intensity polar patterns can be explained very well by the above theory if the scattering matrix $\tilde{S}$ is replaced by the polarizability tensor, which is a scalar for cubic semiconductor. In principle, values of $Q_{\parallel}$ and $Q_{\perp}$ can be obtained from the Rayleigh backscattering data and fitting to Eq. (4.7), or the values can be obtained by field intensity calculation inside infinite long wires, i.e., $(I_{\text{int}}^{\parallel}/I_{\text{int}}^{\perp}) = (Q_{\parallel}^2/Q_{\perp}^2)$.[9] These results will be published elsewhere.[9] In our discussion, we will directly use these results.

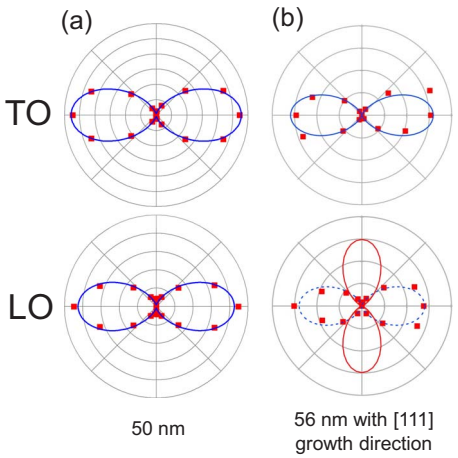

FIG. 6. (Color online) (a) Experimental data for the TO and LO polar plots for a 50-nm wire on Si substrate (unknown growth axis). Solid curves represent fits of a $\cos^4\theta$ to the data. (b) TO and LO antenna polar plots for a 56-nm wire over a hole on a TEM grid; SAD indicates a $\langle 111 \rangle$ growth axis. Data are indicated by the points and solid curves for TO and LO are predictions according to Eq. (4.7). The dashed curve in the LO polar plot is a $\cos^4\theta$ fitting to the data points and is not predicted by theory. For the NW in (b), the theory does not predict the observed LO pattern.

V. EXPERIMENTAL RESULTS IN POLARIZED RAMAN SCATTERING FROM LONG GaP NWS

In this section, we show the experimental polarized Raman-scattering results from individual GaP NWs and compare these results with the theory developed in the previous section. Polarized Raman scattering was carried out on more than 40 GaP NWs with diameters $40 < d < 600$ nm and lengths more than 10 μm. The synthesized GaP NWs were dispersed into isopropanol alcohol by mild ultrasonication and then a drop of NW solution was deposited on either a patterned silicon substrate (100-nm oxide layer) or on a TEM grid (Ted Pella Inc.).

In Figs. 6–10, we display typical experimental Raman polar patterns $I(\theta)$ (dots) for LO and TO backscattering collected from various individual GaP NWs using 514.5-nm excitation. Data in the figures (dots) are taken on wires either suspended over a hole in a TEM grid or supported on a Si substrate. For wires suspended on a Cu TEM grid, the TEM image and selected area diffraction (SAD) pattern were used to determine the wire diameter and the growth axis, respec-

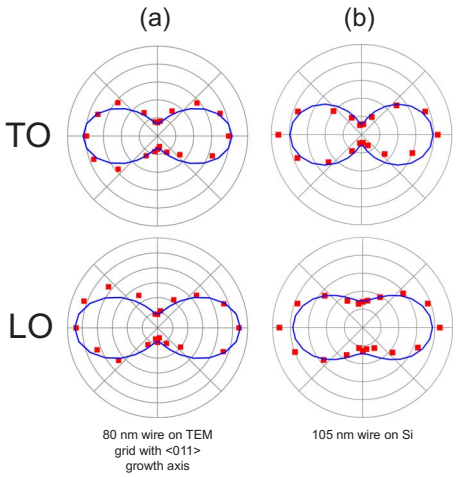

FIG. 7. (Color online) Polar patterns of TO and LO phonons of type I: (a) the wire is on TEM grid with ⟨011⟩ growth direction and is 80 nm, the solid curve is obtained for $Q_\parallel/Q_\perp \approx 1.77$ and $\varphi = 90°$ or 160°; (b) the wire is 105 nm and is on Si substrate, the solid curve is obtained for possible ⟨110⟩ growth axis, $Q_\parallel/Q_\perp \approx 1.42$ and $\varphi = 95°$ or 165°.

tively. For NWs deposited on Si substrates, the diameter was obtained from the height of the wire cross section measured by atomic-force microscope. In this case, the wire-growth direction ⟨*hkl*⟩ is not known. The theoretical curves (solid) are calculated on the basis of Eq. (4.7) using either experimental values of $(Q_\parallel^2/Q_\perp^2)$ (from Rayleigh scattering)[9] or results calculated from the infinite long wire $(I_{\rm int}^\parallel/I_{\rm int}^\perp) = (Q_\parallel^2/Q_\perp^2)$.[9,11]

There are typically four types of Raman-intensity polar patterns observed from the experimental data among more than 40 GaP NWs. Next we discuss each type separately.

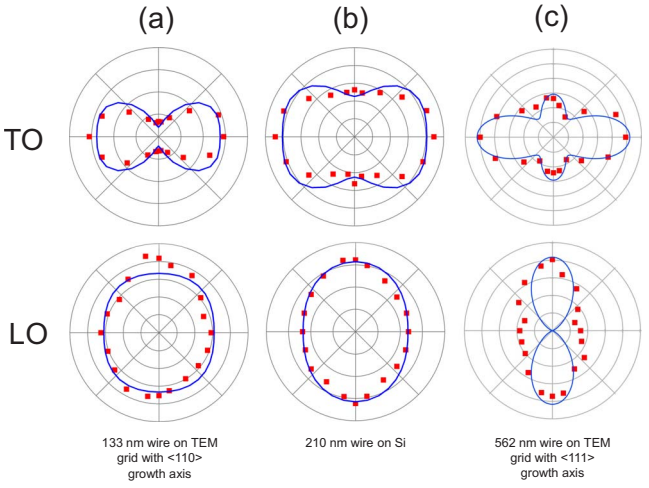

FIG. 8. (Color online) TO and LO intensity polar patterns of type II: (a) a 133-nm wire grew along ⟨110⟩ on TEM grid, the solid curve is obtained for $Q_\parallel/Q_\perp \approx 1.24$ and $\varphi = 105°$ or 175°. (b) a 210-nm wire on Si substrate; the solid curve is obtained for possible ⟨110⟩ growth axis, $Q_\parallel/Q_\perp \approx 0.9$ and $\varphi = 94°$ or 164°; and (c) a 562-nm wire on TEM grid with ⟨111⟩ growth axis; $Q_\parallel/Q_\perp \approx 0.9$ and $\varphi = 0°$, 60°, or 120°.

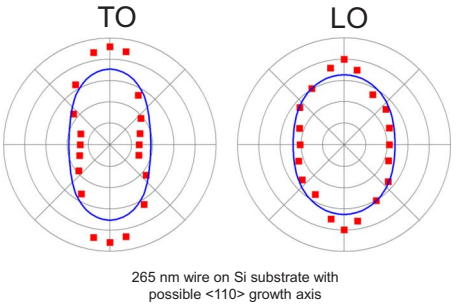

FIG. 9. (Color online) TO and LO intensity polar patterns of type III. The wire is 265 nm on Si substrate with possible ⟨110⟩ growth axis at $Q_\parallel/Q_\perp \approx 0.89$ and $\varphi = 92°$ or 162°.

A. Type I: Both TO and LO intensity patterns are dipole antenna

For GaP NWs with small diameters (<70 nm), both TO and LO are found to act like a nearly perfect dipole antenna that leads to a polarized scattering-intensity function $I(\theta) \sim \cos^4\theta$. The same behavior has been found in the other one-dimensional systems, such as SWNTs,[21,24] 20-nm WS_2 nanotubes.[13] SNWs at antenna resonance exhibit the property $Q_\parallel \gg Q_\perp$. In this case, Eq. (4.7) can be simplified by neglecting terms involving $Q_\perp$. The Raman intensity for SNWs at strong antenna resonance is then

$$I_{\rm NW\ Raman}^{\rm TO,LO} \propto R_{22}^2 Q_\parallel^4 \cos^4\theta, \quad (Q_\parallel \gg Q_\perp;\ \text{any}\ \langle hkl\rangle). \tag{5.1}$$

This is a very important result. It tells us that for transformed LO or TO Raman tensors that exhibit a nonzero R_{22} element, the Raman-intensity polar patterns for these phonons should both follow the $\sim\cos^4\theta$ form. In Fig. 6, we show Raman results for two GaP NWs that exhibit a strong antenna effect for both TO and LO phonon scatterings. The 55-nm wire [Fig. 6(a)] was supported on a Si substrate. If this wire grows along the ⟨110⟩ direction, the R_{22} element for both TO and LO are nonzero and the $\cos^4\theta$ fit agrees with Eq. (5.1). In Fig. 6(b), we show results for a slightly larger diameter $d = 56$ nm GaP NW on TEM grid whose SAD pattern indicates a ⟨111⟩ growth direction. From the results calculated in Sec. V, it can be shown that the transformed Raman tensor of a ⟨111⟩ GaP NW has nonzero $R_{22}^{\rm TO}$ element for all tipping

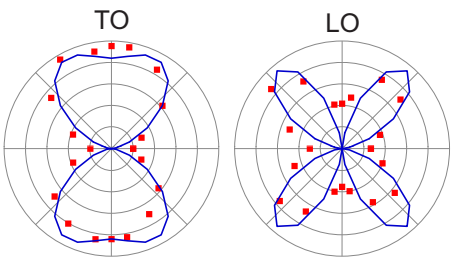

FIG. 10. (Color online) TO and LO polar patterns of type IV: the wire is 265 nm on Si substrate for possible ⟨100⟩ growth axis at $Q_\parallel/Q_\perp \approx 0.89$. The information of rotational angle φ is lost.

angles φ. The $\cos^4\theta$ fit of TO in Fig. 6(b) agrees with Eq. (5.1). However, the transformed LO Raman tensor elements of a GaP ⟨111⟩ NW must satisfy $R_{22}^{\mathrm{LO}}=R_{23}^{\mathrm{LO}}=R_{32}^{\mathrm{LO}}=0$, and $R_{33}^{\mathrm{LO}}\neq 0$. Therefore, from Eq. (4.7), without any restrictions on $Q_{\parallel}$ and $Q_{\perp}$, we have for LO phonons

$$I_{\mathrm{NW\ Raman}}^{\mathrm{LO}} \propto R_{33}^2 Q_{\perp}^4 \sin^4\theta, \quad (\mathrm{For}\langle 111\rangle). \tag{5.2}$$

In Fig. 6(b) of LO, the dashed curve is the $\cos^4\theta$ fitting to LO polar pattern, which is not the theoretical prediction. The rotated solid curve is the predicted LO polar pattern as indicated in Eq. (5.2) for the GaP NW with ⟨111⟩ growth axis. This suggests the possibility that the optical antenna effect dominates for small diameter SNWs and the Raman selection rules were masked.

Similar Raman-intensity patterns were also observed from some other GaP NWs with diameters larger than 70 nm. Figure 7(a) displays the Raman-intensity patterns of an 80-nm wire suspended over a hole in a TEM grid. The wire grew along ⟨011⟩ direction according to the SAD. Both the experimental TO and LO patterns of the $d=80$ nm wire can be described as an "open dipole" (i.e., the patterns are dipolelike and open at the origin); the solid curve is calculated from Eq. (4.7) for a ⟨011⟩ wire with a $Q_{\parallel}/Q_{\perp}\sim 1.77$ (based on the infinite wire calculation) and $\varphi=90°$ or 160°.

In Fig. 7(b), we show the polar patterns of another GaP NW with $d=105$ nm on a Si substrate. Both TO and LO patterns are also dipolelike and open at the origin. However, the center of LO pattern opens more than that of TO pattern. The solid curve is for the possible ⟨110⟩ growth direction with $Q_{\parallel}/Q_{\perp}\sim 1.42$ (infinite long-wire calculation) and $\varphi=95°$ or 165°.

B. Type II: TO is dipolelike while LO is 90° rotated dipolelike

For the $d=133$ nm ⟨011⟩ NW [Fig. 8(a)], the experimental TO pattern is also an open dipole while the experimental LO pattern is nearly elliptical and oriented at 90° with respect to the TO pattern. Our best model calculation (solid curve) for a ⟨011⟩ wire uses $Q_{\parallel}/Q_{\perp}\sim 1.24$ (infinite long-wire calculation) and $\varphi=105°$ or 175°.

Figure 8(b) shows the TO and LO patterns for a $d=210$ nm GaP NW on Si substrate. The solid curve is for $Q_{\parallel}/Q_{\perp}\sim 0.9$ (infinite long-wire calculation) and $\varphi\sim 94°$ or 164° with possible ⟨110⟩ growth axis.

Another example is for a $d=562$ nm wire on TEM grid with ⟨111⟩ growth axis shown in Fig. 8(c). The TO plot is more than an open-dipole pattern. However, it shows an asymmetric open multilobe pattern in which the horizontal lobes are much larger than the vertical ones. The solid curve is for $Q_{\parallel}/Q_{\perp}\sim 0.9$ (from Rayleigh scattering on the same wire) and $\varphi\sim 0°$, 60°, or 120° with ⟨111⟩ growth direction.

C. Type III: Both TO and LO are 90° rotated dipolelike

Figure 9 shows the TO and LO patterns of a $d=265$ nm NWs supported on Si. We observe nearly elliptical LO and TO patterns, both oriented along $\theta=90°$; the solid curve is for a possible ⟨110⟩ wire with $Q_{\parallel}/Q_{\perp}\sim 0.89$ (value from Rayleigh scattering on a wire with the same diameter) and $\varphi\sim 92°$ or 162°.

D. Type IV: TO is 90° rotated dipolelike and LO is quadrupolelike

The polar plots of this type are shown in Figure 10. The wire is also on the Si substrate with $d=265$ nm. The solid curve is for a possible ⟨100⟩ wire with $Q_{\parallel}/Q_{\perp}\sim 0.89$ (value from Rayleigh scattering on a wire with same diameter). We could not derive any information on the angle φ here because the intensity-patterns results from Raman tensor for ⟨100⟩ wire do not change with the angle φ as seen in Fig. 3. Actually, only one polar pattern of this type has been observed. Most probably it is because we seldom found wires with ⟨100⟩ growth directions.

VI. SUMMARY AND CONCLUSIONS

We have systematically studied the polarized first-order TO and LO Raman scattering from GaP NWs with different diameters both experimentally and theoretically. For small-diameter GaP wires ($d<70$ nm), a simple $\cos^4\theta$ polar scattering pattern for both TO and LO phonons is observed disregard the growth axes of GaP NWs. The proposed theory failed to explain this antenna behavior. We believe that the polar patterns are dominated by an optical antenna effect for small wires and the Raman selection rules are masked. As the diameter of the GaP NW increases, some other patterns have been observed. These Raman-intensity polar patterns were quantitatively explained well by a simple theory which stems from the interplay of photon confinement, the NW growth direction and the orientation of the NW crystallographic axes with respect to the incident electric field.

ACKNOWLEDGMENTS

We thank G. Chen for helpful discussion. The financial support of this work was provided by NSF-NIRT (Nanotechnology and Interdisciplinary Research Initiative) under Grant No. DMR-0304178.

*Author to whom correspondence should be addressed.
†juw135@psu.edu
‡duz113@psu.edu
§hur3@psu.edu

[1] W. Lu and C. M. Lieber, Nature Mater. **6**, 841 (2007).
[2] P. J. Pauzauskie and P. Yang, Mater. Today **9**, 36 (2006).
[3] F. Patolsky, B. P. Timko, G. F. Zheng, and C. M. Lieber, MRS Bull. **32**, 142 (2007).
[4] H. Yu, J. Li, R. A. Loomis, L.-W. Wang, and W. E. Buhro, Nature Mater. **2**, 517 (2003).
[5] A. D. Yoffe, Adv. Phys. **51**, 799 (2002).
[6] K. W. Adu, H. R. Gutiérrez, U. J. Kim, G. U. Sumanasekera, and

P. C. Eklund, Nano Lett. **5**, 409 (2005).
[7] A. P. Alivisatos, Science **271**, 933 (1996).
[8] K. J. Vahala, Nature (London) **424**, 839 (2003).
[9] D. M. Zhang, J. Wu, Q. J. Lu, H. R. Gutierrez, and P. C. Eklund (unpublished).
[10] L. Y. Cao, B. Nabet, and J. E. Spanier, Phys. Rev. Lett. **96**, 157402 (2006).
[11] G. Chen, J. Wu, Q. Lu, H. R. Gutierrez, Q. Xiong, M. E. Pellen, J. S. Petko, D. H. Werner, and P. C. Eklund, Nano Lett. **8**, 1341 (2008).
[12] J. Wu, A. K. Gupta, H. R. Gutierrez, and P. C. Eklund, Nano Lett. **9**, 3252 (2009).
[13] P. M. Rafailov, C. Thomsen, K. Gartsman, I. Kaplan-Ashiri, and R. Tenne, Phys. Rev. B **72**, 205436 (2005).
[14] T. Livneh, J. Zhang, G. Cheng, and M. Moskovits, Phys. Rev. B **74**, 035320 (2006).
[15] M. S. Dresselhaus, G. Dresselhaus, and A. Jorio, J. Phys. Chem. C **111**, 17887 (2007).
[16] M. S. Dresselhaus, G. Dresselhaus, R. Saito, and A. Jorio, Phys. Rep. Rev. Sec. Phys. Lett. **409**, 47 (2005).
[17] Q. Xiong, R. Gupta, K. W. Adu, E. C. Dickey, G. D. Lian, D. Tham, J. E. Fischer, and P. C. Eklund, J. Nanosci. Nanotechnol. **3**, 335 (2003).
[18] R. Gupta, Q. Xiong, G. D. Mahan, and P. C. Eklund, Nano Lett. **3**, 1745 (2003).
[19] R. Loudon, Adv. Phys. **50**, 813 (2001).
[20] P. Y. Yu and M. Cardona, *Fundamentals of Semiconductors: Physics and Materials Properties* (Springer, Berlin, New York, 2001).
[21] G. S. Duesberg, I. Loa, M. Burghard, K. Syassen, and S. Roth, Phys. Rev. Lett. **85**, 5436 (2000).
[22] H. Chew and D. S. Wang, Phys. Rev. Lett. **49**, 490 (1982).
[23] M. Cardona and R. Merlin, *Light Scattering in Solids. IX, Novel Materials and Techniques* (Springer, Berlin, New York, 2007).
[24] A. Jorio, A. G. Souza Filho, V. W. Brar, A. K. Swan, M. S. Ünlü, B. B. Goldberg, A. Righi, J. H. Hafner, C. M. Lieber, R. Saito, G. Dresselhaus, and M. S. Dresselhaus, Phys. Rev. B **65**, 121402(R) (2002).